ACS APPLIED MATERIALS & INTERFACES

www.acsami.org

Research Article

Thermal Interface Enhancement via Inclusion of an Adhesive Layer Using Plasma-Enhanced Atomic Layer Deposition

Heungdong Kwon,[⊥] Christopher Perez,[⊥] Hyojin K. Kim, Mehdi Asheghi, Woosung Park, and Kenneth E. Goodson*

Cite This: https://doi.org/10.1021/acsami.0c19197

Read Online

ACCESS | Metrics & More | Article Recommendations | Supporting Information

ABSTRACT: Interfaces govern thermal transport in a variety of nanostructured systems such as FinFETs, interconnects, and vias. Thermal boundary resistances, however, critically depend on the choice of materials, nanomanufacturing processes and conditions, and the planarity of interfaces. In this work, we study the interfacial thermal transport between a nonreactive metal (Pt) and a dielectric by engineering two differing bonding characters: (i) the mechanical adhesion/van der Waals bonding offered by the physical vapor deposition (PVD) and (ii) the chemical bonding generated by plasma-enhanced atomic layer deposition (PEALD). We introduce 40-cycle (~2 nm thick), nearly continuous PEALD Pt films between 98 nm PVD Pt and dielectric materials (8.0 nm TiO_2/Si and 11.0 nm Al_2O_3/Si) treated with either O_2 or O_2 + H_2 plasma to modulate their bonding strengths. By correlating the treatments through thermal transport measurements using time-domain thermoreflectance (TDTR), we find that the thermal boundary resistances are consistently reduced with the same increased treatment complexity that has been demonstrated in the literature to enhance mechanical adhesion. For samples on TiO_2 (Al_2O_3), reductions in thermal resistance are at least 4% (10%) compared to those with no PEALD Pt at all, but could be as large as 34% (42%) given measurement uncertainties that could be improved with thinner nucleation layers. We suspect the O_2 plasma generates stronger covalent bonds to the substrate, while the H_2 plasma strips the PEALD Pt of contaminants such as carbon that gives rise to a less thermally resistive heat conduction pathway.

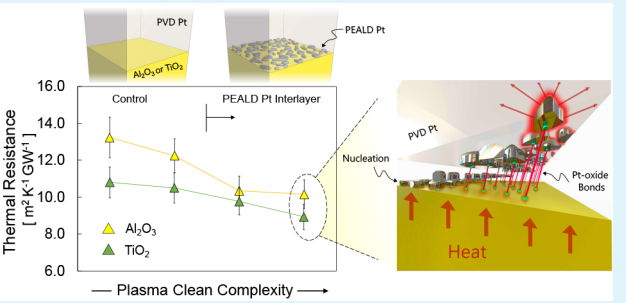

KEYWORDS: *atomic layer deposition, time-domain thermoreflectance, bonding strength, thermal boundary conductance, plasma treatment, platinum, nucleation layer*

INTRODUCTION

The progress toward the low dimensional limits of electronic devices has made it increasingly difficult to control operating temperatures due to hot spots that accompany faster switching speeds and greater current densities.[1,2] Technologies in bolometry,[3] temperature sensing,[4] and, of course, microelectronics[5] are composed of either metal interconnects, passivation layers, or thin-film dielectrics whose dissipation of heat is limited by phonon scattering at boundaries. In the same way thermal conductivity (κ) governs heat transfer in bulk materials, the thermal boundary conductance (G) dominates thermal dissipation in many thin-film systems and 2D semiconductor devices, with temperature drops across interfaces comparable to that across the materials themselves.[1,6,7] Understanding and controlling G is thus critical and a major challenge for improving the performance of thin-film and nanostructured material systems.

The consensus in the heat transfer community is that greater surface energies resulting from stronger chemical bonds (e.g., covalent bonds) offer more effective heat conduction across interfaces than their weaker-bond counterparts.[8−13] This concept has been upheld by studies that varied termination chemistries in self-assembled monolayers (SAMs),[10] changed the termination chemistry on the surface of synthetic diamond interfaces,[8] chemically functionalized graphene surfaces with adsorbates,[9] and bridged interfaces with covalently bonded organic molecules.[11,12] All investigations showed a positive correlation between bond strength and thermal transport, with a typically 2-fold increase in G that is often facilitated with some form of plasma exposure.

Despite research focus on surface enhancement, little attention has been placed on tuning G with deposition techniques that can capitalize on increasing bond strength.[14,15] Plasma-enhanced atomic layer deposition (PEALD) is one such method, quickly becoming an essential tool because of its

Received: November 10, 2020
Accepted: March 12, 2021

extreme control over the thickness and composition of thin films that can integrate into CMOS compatible platforms.[16−18] PEALD can also mitigate nonideal nucleation behavior that can arise from high surface energy materials such as Pt, a noble metal used for high aspect ratio via passivation,[18] bolometry,[3] and numerous other applications.[19,20] Although Pt suffers from poor wettability and adhesion to oxides,[21] in situ O_2 plasma during deposition has been shown to enhance chemisorption and oxidation by directly supplying O to the substrate surface.[22] This enables the ability to support ultrathin film Pt growth on account of the increased bond strength of chemisorbed O on Pt.[22−24] Furthermore, the reduction of Pt precursors from H_2 plasma has been observed to yield smaller clusters of Pt adatoms that contain fewer carbon contaminants, known to contribute to poor film adhesion.[25] Less carbon impurities result in higher cluster−surface bonding energies compared to traditional thermal decomposition of the precursors.[26] Although the systematic quantification of these treatments on mechanical adhesion is lacking, tape lift-off and double cantilever beam tests performed at Stanford University reveal a promising trend that motivate this study: in situ O_2 + H_2 plasma during PEALD increases the peel strength (see the Supporting Information Section S4 and Figure S3). If PEALD Pt can offer strong bonding energy, using it as an interlayer can potentially enhance interfacial heat transfer in a tunable way by adjusting the reaction chemistry between precursors, plasma treatments, and the surface onto which Pt nucleates.

Though the addition of material between interfaces (Figure 1a) traditionally introduces more thermal resistance ($R_{th} = G^{-1}$), the unique Volmer−Weber growth[27,28] of PEALD Pt can challenge this notion. The competing effects of increased bond strength, more thermal mass, and changes in surface area play complex roles in describing thermal transport. However, the growth evolution of PEALD Pt on various substrates suggests a critical cycle count where the surface-to-volume of the particles is maximized, informed by the evolution of Pt surface coverage on the substrate[29] seen in Figure 1b. Indeed, an augmented surface area offered by nucleating Pt particles may translate into more area for heat transfer, long known in extended surface applications and observed recently in nanopatterned structures.[30] At larger cycle counts, however, the Pt particles would coalesce into a continuous film with a thermal resistance proportional to its thickness. Thus, a cycle-dependent R_{th} is expected in early stage nucleating films, with a minimum value at a cycle range of approximately 40−60 cycles.[29]

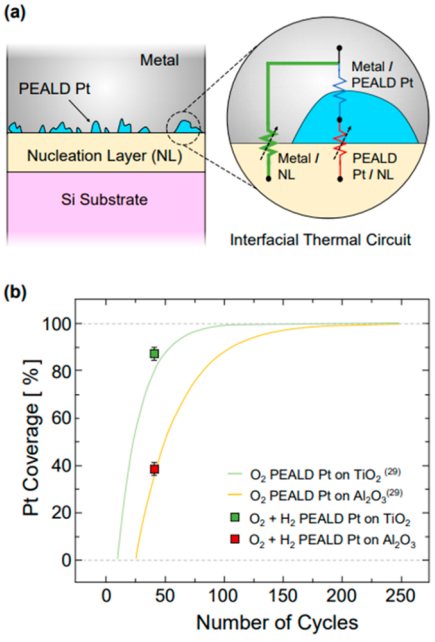

Figure 1. (a) On the left is a simplified planar schematic depicting an ultrathin film of nucleating PEALD Pt between a nucleation layer [NL] and an Si substrate, both covered by metal. On the right is a thermal circuit diagram illustrating the thermal resistances involved with a PEALD Pt interlayer at a metal/Si interface. (b) The evolution of Pt surface coverage on the substrate with respect to cycle count. The solid lines represent a regression to experimental data for O_2 PEALD Pt,[29] while the squares denote the calculated area coverage for the O_2 + H_2 PEALD Pt films in this work.

In this work, we study the interfacial thermal transport between a nonreactive metal (Pt) and a dielectric by engineering two differing bonding characters: (i) the mechanical adhesion/van der Waals bonding offered by the physical vapor deposition (PVD) and (ii) the chemical bonding generated by PEALD. We introduce 40-cycle (∼2 nm thick), nearly continuous PEALD Pt films between 98 nm PVD Pt and dielectric materials (8.0 nm TiO_2/Si and 11.0 nm Al_2O_3/Si) treated with either O_2 and O_2 + H_2 to modulate their effect on cross-plane thermal transport. We experimentally correlate these conditions through thermal measurements using time-domain thermoreflectance (TDTR), revealing a substantial increase in G with the addition of a 40-cycle PEALD Pt interlayer deposited with O_2 + H_2 plasma treatments that lend themselves well in the PEALD of TiO_2 and Al_2O_3.

EXPERIMENTAL SECTION

In this section, we describe the preparation of our PEALD samples and proceed to report the details of our TDTR facility as well as our thermal model to describe our material systems.

Sample Preparation. We prepared 8.0 nm (150 cycles) TiO_2 and 11.0 nm (100 cycles) Al_2O_3 films deposited using PEALD (Cambridge Nanotech Fiji, F202) on (100) Si substrates that were dipped in diluted hydrofluoric acid to remove as much native oxide as possible prior to deposition. The thicknesses were measured by using ellipsometry (Woollam M2000). The precursors used were tetrakis-(dimethylamido)titanium(IV) and trimethylaluminum for TiO_2 and Al_2O_3, respectively, with O_2 plasma as the coreactant.[29,31,32] The deposition temperature was 200 °C, and the plasma power was set to 300 W. The literature suggests that 150-cycle ALD TiO_2 films with deposition temperatures as high as 260 °C are amorphous.[33] Additionally, 8 nm of ALD Al_2O_3 has been reported to crystallize only after a deposition temperature of 900 °C is reached.[34] Thus, our films are considered to be in the amorphous phase.

Following the deposition of TiO_2 and Al_2O_3 on Si, samples were diced into several chips and subjected to four treatments, summarized in Figure 2a. Sample C1 was used as a control, with only an as-deposited nucleation layer atop Si. Sample C2 received a 900 s in situ O_2 plasma clean within the PEALD chamber before and after the deposition of the nucleation layer. Samples C3 and C4 had a PEALD Pt film deposited by using 40 cycles atop the nucleation layer, in addition to the 900 s in situ O_2 plasma pre- and postclean. However, these were treated with either an O_2 or O_2+H_2 plasma with each cycle. Figure 2b illustrates the difference between the O_2 and O_2+H_2 plasma treatments with respect to the PEALD of Pt by using a trimethyl(methylcyclopentadienyl)platinum(IV) or $MeCpPtMe_3$ precursor. Although such a low cycle count produces Volmer−Weber growth,[27,28] the approximate growth rate of 0.5 Å/s (see Supporting Information Section S1) yields a PEALD Pt film equivalent to roughly 2 nm in thickness.

https://doi.org/10.1021/acsami.0c19197
ACS Appl. Mater. Interfaces XXXX, XXX, XXX−XXX

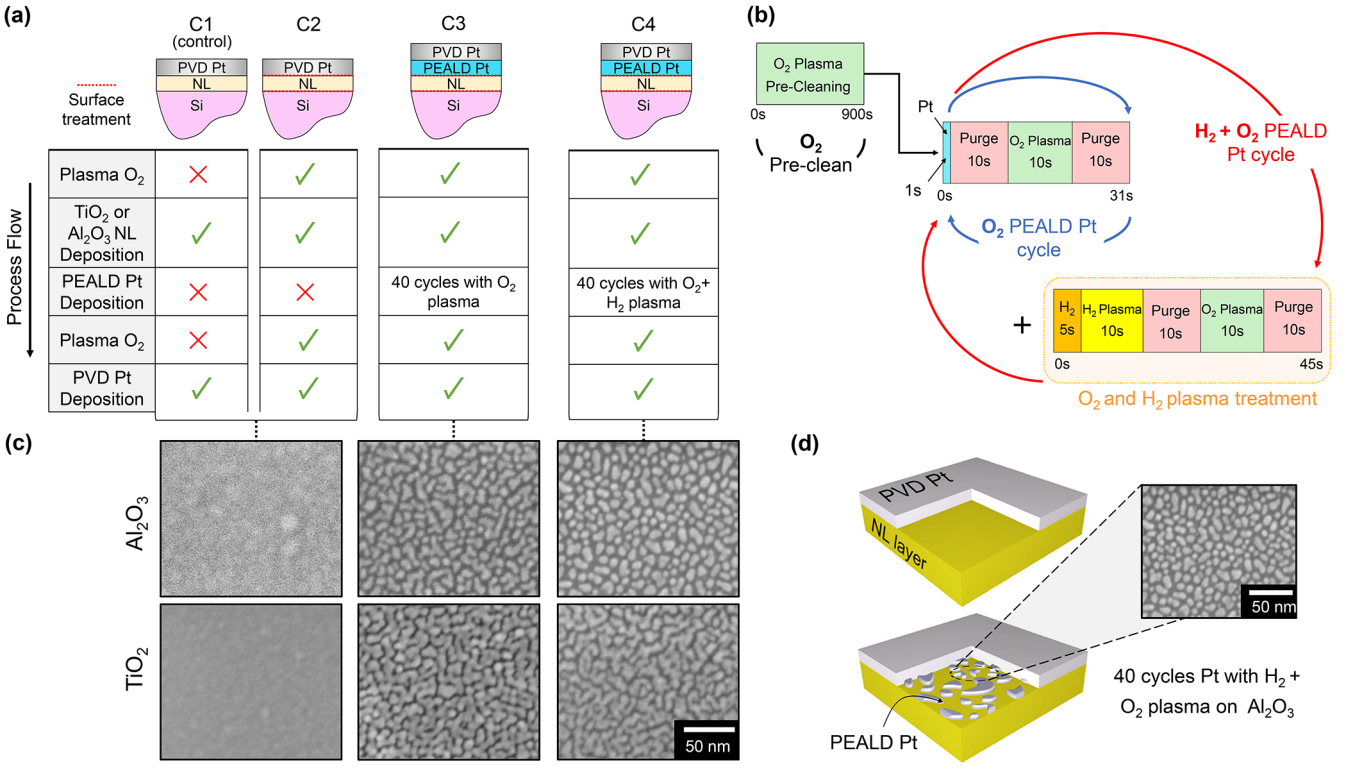

Figure 2. (a) Eperimental conditions with respect to process control and nucleation layer [NL], either TiO_2 or Al_2O_3. (b) A complete cycle schematic for the O_2+H_2 plasma PEALD Pt process (red loop) that emphasizes the departure from an O_2 plasma PEALD process (blue loop). (c) Scanning electron micrographs (SEMs) of the top surfaces of TiO_2 and Al_2O_3 for the experimental conditions. (d) An illustration of the augmented contact area due to the nucleating "islands" of Pt during the PEALD process.

After the samples were removed from vacuum, scanning electron microscopy (SEM) (FEI Nova NanoSEM 450) was used to image the top surface of the samples (Figure 2c). X-ray photoelectron spectroscopy data (XPS, PHI 124 5000 VersaProbe III, Ulvac-PHI, Inc.) were used to confirm chemical composition on all PEALD Pt films deposited with O_2 and O_2+H_2, for both TiO_2 and Al_2O_3 nucleation layers. We also contrast this data with the XPS spectra generated for our 98 nm thick PVD (evaporated) Pt layers (see Figure S2). For 40 cycles of O_2 PEALD Pt on TiO_2 and Al_2O_3 nucleation layers, the binding energy peaks are slightly shifted to higher energies compared to the PVD Pt, suggesting oxidized Pt exists within 40 cycles of O_2 PEALD Pt. Interestingly, the peaks of O_2+H_2 PEALD Pt are shifted less from those of O_2 PEALD Pt. A 98 nm Pt film was deposited on top of all the samples with electron beam evaporation (AJA International Inc., ATC-E Series). The thickness of the PVD Pt films was determined via SEM. PVD Pt defined the metallization in our metal-oxide configuration and facilitated TDTR measurements by acting as an optothermal transducer.

Thermal Characterization. Time-domain thermoreflectance (TDTR) is an ultrafast optical pump−probe technique for measuring the thermophysical properties of both bulk and thin film materials. The details of this method and our experimental facility are provided elsewhere.[35,36] To summarize, thermoreflectance data are fit to the solution of a 3D heat diffusion model for a multilayer stack of materials, and the unknown properties of interest are used as parameters to converge measurement and theory.[37] Measurements were taken at a pump beam modulation frequency (f_{mod}) of 10 MHz. Using a knife-edge technique, beam diameters of 5.5 and 3.1 ± 0.05 μm were measured for the pump and probe, respectively.

Simplifying assumptions were made for the PEALD Pt to attain an idealized model of the physical system shown in Figure 3. We neglect the interface between the PVD Pt and the underlying PEALD Pt due to the order of magnitude increase in G that comes with metal−metal contact compared to typical metal−dielectric interfaces.[38] Additionally, the ∼2 nm thick PEALD Pt film was likely not continuous, rather

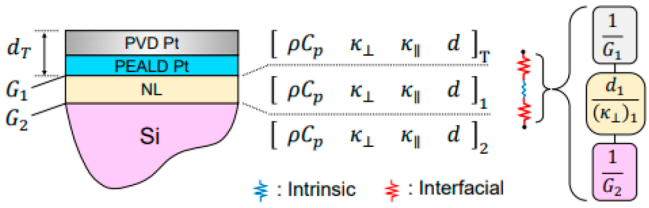

Figure 3. Thermal model for the PEALD samples, consisting of four materials modeled as three layers: 98 nm of PVD Pt + 40 cycles of PEALD Pt, an 8.0 nm TiO_2 or 11.0 nm Al_2O_3 nucleation layer, and an Si substrate. Each layer is described by five physical parameters: the volumetric heat capacity (ρC_p), the cross- and in-plane thermal conductivities ($\kappa_\perp$ and $\kappa_\parallel$), the layer thickness (d), and the thermal boundary conductance ($G = R^{-1}$) to the next layer. The parameter values are listed in Table 1.

containing islands of nucleating Pt.[27−29] In addition, sensitivity analysis of our TDTR signal (see the Supporting Information Section S5 and Figure S4) reveals the coupled nature of $(\rho C_p)_{PEALD\ Pt}$ and $(d)_{PEALD\ Pt}$, making the thermal mass $(\rho C_p d)$, and therefore the thickness of PEALD Pt, a significant contribution to the TDTR signal. The final sample configuration is composed of three layers: the combined PVD Pt and PEALD Pt, a nucleation layer (TiO_2 or Al_2O_3), and a Si substrate. The PEALD nucleation layers are extremely thin and limit the measurable properties of the physical system.[45] This is because in the limiting case of zero film thickness, the G's govern the total thermal resistance, $R_{th} = G^{-1}$. In turn, the TDTR measurement is most sensitive to the G's on either side of the nucleation layer. It is difficult, however, to decouple these due to deep thermal penetration δ_p of the modulated by pump beam compared to the nucleation layer thicknesses. For example, at a modulation frequency f_{mod} = 10 MHz, κ = 2.5 W m^{-1} K^{-1}, and ρC_p = 2.8 MJ m^{-3} K^{-1}, the thermal penetration is $\delta_p = \sqrt{\kappa/(\pi \rho C_p f_{mod})} \approx 170$ nm.

https://doi.org/10.1021/acsami.0c19197
ACS Appl. Mater. Interfaces XXXX, XXX, XXX−XXX

Table 1. Parameters Used to Determine the Effective Thermal Resistances $R_{th,eff}$ of the PEALD Samples via a Two-Parameter Fit of $\kappa_{\perp,eff}$ and d_T[a]

material	ρC_p [MJ m^{-3} K^{-1}]	$\kappa_\perp$ [W m^{-1} K^{-1}]	$\kappa_\perp/\kappa_\parallel$	d [nm]	$R_{th,i} = d/\kappa_\perp$ [m^2 KGW^{-1}]
Pt/PEALD Pt	2.83 ± 0.01[39,40]	62.10 ± 3.10	1	$d_T \pm \sigma$	
TiO_2	2.98 ± 0.30[41,42]	2.52 ± 0.07[42]	1	8.0 ± 0.5	3.17 ± 0.29
Al_2O_3	2.13 ± 0.21[41,42]	2.13 ± 0.15[43]	1	11.0 ± 0.5	5.16 ± 0.60
Si	1.66 ± 0.09[44]	124.6 ± 10.0	1	1×10^5	

[a]Intrinsic thermal conductivities of the nucleation layers were taken from the literature to provide intrinsic thermal resistances $R_{th,i}$ to quantify interfacial conduction enhancement.

Sensitivity analysis considering the TiO_2 sample demonstrates the dominance of the signal to $R_{th,eff}$, realized as an effective cross-plane thermal conductivity $\kappa_{\perp,eff}$ (see the Supporting Information Section S5 and Figure S4). Thus, we determine an effective $R_{th,eff}$ that is composed of the intrinsic $\kappa_\perp$ of the nucleation layer and the R_{th}'s from PEALD Pt−nucleation layer and nucleation layer−Si interfaces. Applying a series resistor model that treats $R_{th,eff}$ as a summation of the film and interfacial contributions yields[46]

$$R_{th,eff} = \frac{1}{G_{PEALDPt-NL}} + \frac{d_{NL}}{\kappa_{\perp,NL}} + \frac{1}{G_{NL-Si}} = \frac{d_{NL}}{\kappa_{\perp,eff}} \quad (1)$$

where the subscript "NL" refers to the nucleation layer. The measured $R_{th,eff}$ can then reveal the effect of surface treatments assuming the intrinsic κ of the nucleation layer and the R_{th} between the nucleation layer and the Si substrate remain unchanged. We note that separating the interfaces from the material volumes by using eq 1 is justified given the amorphous nature of ALD thin films, yielding isotropic transport conditions within the films.

We can infer the effects of conditions C1−C4 in Figure 2a on the thermal interface properties between the PVD Pt and nucleation layer by performing a two-parameter fit of $\kappa_{\perp,eff}$ and $d_{Pt/PEALD\ Pt} = d_T$. This fitting routine accounts for the nearly continuous ultrathin PEALD Pt layer, removing the need to formulate an effective or average thickness. Others have approximated thin films as an R_{eff} if their thermal time constant is shorter than the heating period for the measurement.[47,48] With regard to a thin film as an R_{eff}, however, can lead to unphysical fitting results since the TDTR response is greatly sensitive to the thermal mass of the transducer at short probe time delays (<1000 ps). At these time scales, the thermal resistance immediately beneath the transducer layer is being probed, and any present material becomes a prime factor in the accuracy of the fitting results.

The parameters used for determining the thermal properties of the PEALD samples are summarized in Table 1 and include the intrinsic nucleation layer κ estimates from the literature.[42,43] The low measured thermal conductivity of Si with TDTR was attributed to probing the onset of nondiffusive transport based on our beam diameters and pump modulation frequency.[49]

RESULTS AND DISCUSSION

Figure 4a visually emphasizes the condition location on the material stack. The results for the two-parameter fitting of $\kappa_{\perp,eff}$ and d_T were converted to effective thermal resistances $R_{th,eff}$ by using eq 1 and are listed in Table 2. The results for TiO_2 and Al_2O_3 are also shown visually in Figures 4b and 4c, respectively. Uncertainty was determined from those of the controlled parameters and the residuals between data and model, the values of which are reported as standard errors. The uncertainties from the thickness of the nucleation layer and the volumetric heat capacity of the Si substrate contributed the most to the total uncertainty of our measurements (see the Supporting Information Section S6 and Table S2).

Conditions C1−C2. We determine the effect of a 900 s O_2 plasma precleaning process on the nucleation layer surface (condition C2). There is a general decrease in $R_{th,eff}$ with O_2 plasma for both TiO_2 and Al_2O_3, attributed to the improved surface quality with an additional O_2 plasma preclean. Such treatments remove surface carbon that intensifies interfacial vibrational mismatch,[50] greatly reducing $R_{th,eff}$. Having been linked to poor film adhesion,[25] removing adventitious carbon with O_2 plasma is commonly performed to improve the adhesion of noble metals to substrates. With no increase in $R_{th,eff}$ with O_2 plasma, we also confirm both materials as being oxygen barriers, i.e., no additional oxide formation within the Si substrate.[42] We note, however, the improvement with the O_2 plasma preclean process was more pronounced for Al_2O_3 than for TiO_2.

Conditions C2−C3. In addition to the O_2 plasma preclean, the introduction of 40 cycles of O_2 PEALD Pt between the

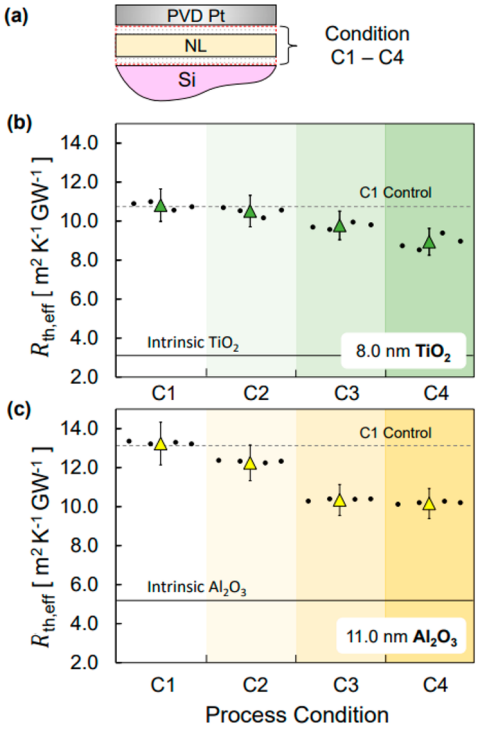

Figure 4. (a) The sample configuration demonstrating the modulation of the PVD Pt−nucleation layer [NL] interface with process conditions C1−C4 detailed in Table 2. The effective thermal resistance $R_{th,eff}$ across the (b) TiO_2 and (c) Al_2O_3 samples measured with TDTR. Each point represents the average of four measurement locations on each sample, seen as black dots. Uncertainty is propagated by summing the contributions of the assumed thermal properties of the film stack, the sample dimensions, the model/data residuals, and the optical parameters used in TDTR setup, listed in Table 1. The dashed horizontal lines emphasize the $R_{th,eff}$ of the C1 control for comparison to the other conditions, while the solid horizontal lines represent the intrinsic thermal resistance for either TiO_2 or Al_2O_3 included in Table 1.

https://doi.org/10.1021/acsami.0c19197
ACS Appl. Mater. Interfaces XXXX, XXX, XXX−XXX

Table 2. Measured R_{th} Results for Conditions C1−C4 as Well as Their Thermal Boundary Resistance Values, $R_{th,B} = R_{th,eff} - R_{th,i}$

condition	nucleation layer	$R_{th,eff}$ [m^2 KGW^{-1}]	$R_{th,B}$ [m^2 KGW^{-1}]
	treatment details	TiO_2/Al_2O_3	TiO_2/Al_2O_3
C1	no treatment	10.82 ± 0.83/ 13.24 ± 1.09	7.65 ± 1.12/ 8.07 ± 1.69
C2	900 s O_2 plasma	10.52 ± 0.81/ 12.24 ± 0.92	7.35 ± 1.10/ 7.08 ± 1.52
	900 s O_2 plasma		
C3	40 cycles of O_2 plasma PEALD Pt	9.78 ± 0.73/ 10.34 ± 0.80	6.61 ± 1.02/ 5.18 ± 1.40
	900 s O_2 plasma		
C4	40 cycles of O_2+H_2 plasma PEALD Pt	8.94 ± 0.69/ 10.16 ± 0.77	5.77 ± 0.98/ 5.00 ± 1.37

PVD Pt layer and the nucleation layers (condition C3) provided a further decrease in $R_{th,eff}$. This improvement was slight for TiO_2 given the measurement uncertainty. Much thinner nucleation layer films are required to improve the sensitivity of the measurements. However, the improvement is markedly larger for Al_2O_3, reducing $R_{th,eff}$ by at least 9% and as much as 40% compared to the control (condition C1).

Conditions C3−C4. By inclusion of H_2 plasma in each O_2 PEALD Pt cycle (condition C4), $R_{th,eff}$ was only marginally reduced, with the TiO_2 improvement was slightly larger than that of Al_2O_3. Compared to the C1 control, the $R_{th,eff}$ reduction is at least 4% but could be as large as 34% for TiO_2. Similarly, $R_{th,eff}$ was reduced for Al_2O_3 by at least 10% but could be as large as 42% given measurement uncertainties. For more insight, we use the intrinsic thermal resistance ($R_{th,i}$) values for the nucleation layers in Table 1 and subtract their contribution to $R_{th,eff}$ for C1 as a baseline quantity. We find that the purely interfacial contributions to the thermal resistance ($R_{th,B}$) for TiO_2 and Al_2O_3 are 7.65 ± 1.12 and 8.07 ± 1.69 m^2 KGW^{-1} for condition C1. With condition C4, however, these were reduced to 5.77 ± 0.98 and 5.00 ± 1.37 m^2 KGW^{-1} for TiO_2 and Al_2O_3, respectively. We suspect that at least such interfacial resistance improvements must exist since our estimates consider the uncertainties in the assumed dielectric material properties and are thus conservative.[42] The C1 condition $R_{th,B}$ values are in close agreement with those in the literature by using similar deposition methods, despite different metallization layers (Al as opposed to Pt).[41−43]

Figure 5a illustrates our experimental $R_{th,B}$ values for both the C1 and C4 conditions along with values found in the literature. For insight into the mechanisms that lead to these trends in R_B's, we contrast our measurements with predictions from the diffuse mismatch models (DMM)[51,52] with a Born−von Karman (BVK) phonon dispersion approximation. The DMM thermal boundary conductance (GDMM) from material A to B is given by

$$G_{A\to B} = \frac{1}{4}\sum_j \int_0^\infty v_{A,j}\hbar\omega D_A(\omega)\frac{\partial f_{BE}^0(\omega, T)}{\partial T}\alpha_{A\to B}\, d\omega \quad (2)$$

where j is the phonon branch, $\alpha_{A\to B}$ is the transmissivity from material A to B, f_{BE}^0 is the Bose−Einstein equilibrium function, and D_A is the phonon density of states in material A. We approximate $v_{A,j}$, the phonon velocity in material A for the jth phonon branch, by fitting experimental data for the phonon dispersion relationship obtained in certain symmetry directions by considering interactions of an atom with its neighbors.[53]

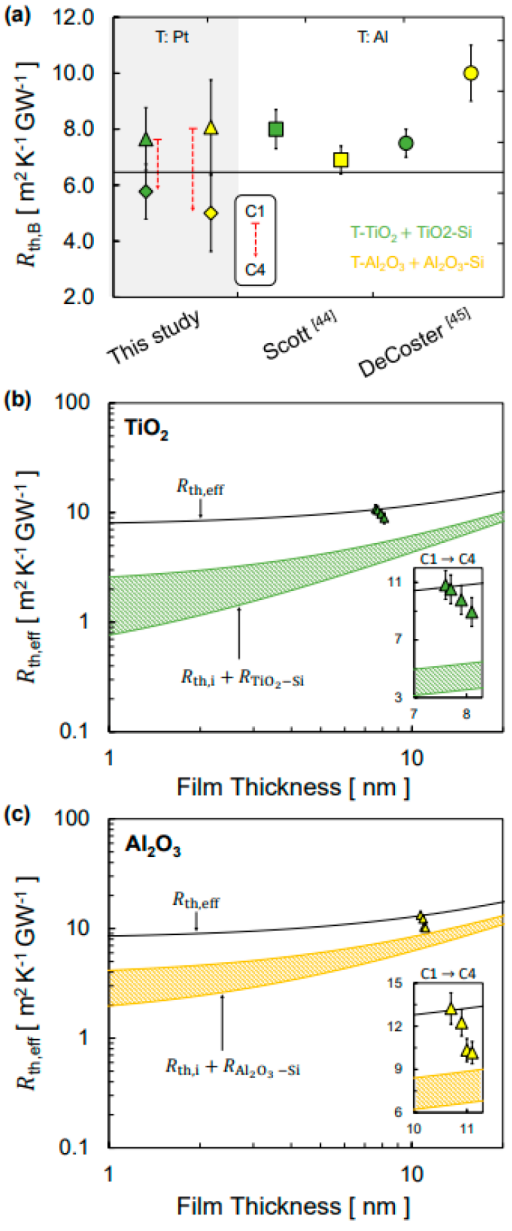

Figure 5. (a) Measured thermal boundary resistances $R_{th,B}$ for conditions C1 (triangles) and C4 (diamonds) compared with literature values for ALD TiO_2 and Al_2O_3. The horizontal black line represents the lower bound $R_{th,B}$ values taken for condition C1 to further emphasize the improvement in thermal boundary conductance. Discrepancies between our data and the literature are attributed to the contrasting metallic transducer (Al vs Pt) in our experiments, denoted by "T". Experimental data of the C1−C4 conditions fit against the thermal circuit model in eq 1 (black line) for (b) TiO_2 and (c) Al_2O_3, where the inset plots are shifted laterally for clarification.

Relative improvements in $R_{th,eff}$ are compared by evaluating eq 1 as a function of dielectric film thickness, seen as the black lines in Figure 5b,c. These include the total thermal resistance due to the Pt/film interface, the film, and the film/Si interface. We approximate the contribution from the film/Si interface by subtracting a range of Pt/film interface values corresponding to

https://doi.org/10.1021/acsami.0c19197
ACS Appl. Mater. Interfaces XXXX, XXX, XXX−XXX

1/2 and 1/3 of the maximum conductance across the interface. By setting the transmission coefficient in the DMM to unity,[54] the maximum conductances were determined to be $G_{max,Pt-TiO_2}$ = 275 and $G_{max,Pt-Al_2O_3}$ = 457 MW m^{-2} K^{-1}. This range is representative of the literature for metal/dielectric interfaces.[42] We find that the effect of the C1−C4 condition is considerable for both films but is once again more pronounced for Al_2O_3. The enhancement in Al_2O_3 causes $R_{th,eff}$ to approach $R_{th,i}$ + $R_{Al_2O_3-Si}$, almost eliminating the thermal resistance from the Pt/Al_2O_3 interface. The heat transfer improvements across the PVD Pt−dielectric interfaces cannot be explained by traditional DMM and lead us to consider the nearly continuous nature of the PEALD Pt films. The films are suspected to provide additional heat conduction pathways due to an augmented contact area, shown schematically in Figure 2d. An ultrathin PEALD Pt film of 40 cycles offers more surface area than a continuous film due to its structure comprising of nucleating islands.[28] To quantify this enhancement, we adapt RMS roughness values of 0.45 and 0.30 nm for 40 cycles of O_2 PEALD Pt on TiO_2 and Al_2O_3 from the literature.[29] This is reasonable given that the observed morphology between the O_2 and O_2+H_2 varieties of PEALD of Pt were identical, seen in Figure 3c. Using these images, we decoupled the Pt film islands from the underlying substrate and find good agreement with the literature for similar PEALD Pt deposition conditions (Figure 1b), yielding Pt:nucleation layer areal enhancements of ∼3% for TiO_2 and ∼15% for Al_2O_3. This also in agreement with the observed experimental C2−C3 conditions (adding an O_2 plasma PEALD Pt interlayer), which experienced at least ∼4% and ∼10% decreases in $R_{th,eff}$ for TiO_2 and Al_2O_3, respectively. The smaller areal enhancement in TiO_2 is ascribed to the higher surface concentration of hydroxyl bonds compared to Al_2O_3, which serve as nucleation sites for the Pt and result in a more continuous film. The areal improvement may explain the reduction in thermal resistance for the lower bound of enhancement but may account for much less if considering the entire possible range. If relaxing the data to a 90% confidence level, for example, the decreasing trend in the C3−C4 $R_{th,eff}$ evolution of TiO_2 suggests another mechanism at play since the morphologies are identical.

The possibility of other heat transfer mechanisms besides an augmented area points us to investigate chemical processes such as adhesion. For example, the DMM predicts lower-limit values of $(R_{th,eff})_{TiO_2}$ = 9.39 and $(R_{th,eff})_{Al_2O_3}$ = 11.38 m^2 KGW^{-1}. It is well-known, however, that the DMM fails to capture atomic-scale interface characteristics, of which we believe interfacial bonding strength to have played a major role. Predictions from molecular dynamics simulations, for example, have provided insight into these effects by tuning chemical potentials between interacting particles at interfaces. Such studies have often revealed variations of boundary resistances of over an order of magnitude in metal−dielectric interfaces due to adhesion effects.[55−58] Although not as appreciable as these more complex simulations predict, our results demonstrate the conceivable heat conduction enhancement that may be attributed to the chemical mechanisms in PEALD.

To understand the possible decrease in thermal resistance, we consider the interfacial chemistry between the O_2 plasma, H_2 plasma, and PEALD Pt interlayer during deposition. Condition C3 describes the PEALD Pt interlayer deposited with O_2 plasma—a treatment that has been shown to directly supply O to the substrate surface and increase the bond strength of chemisorbed O on Pt by enhancing chemisorption and oxidation.[22−24] The increased Pt and O bond strength translates into a decrease in both O and Pt adatom mobility, decreasing nanoparticle size and preventing configurations with low interface energy. This is reinforced by our XPS analysis, where all samples with 40 cycles of PEALD Pt possessed a slight shift to higher binding energies compared to our PVD Pt, suggesting oxidized Pt exists within our interlayer films (Supporting Information Section S3). The additional H_2 plasma in each PEALD Pt cycle (condition C4), on the other hand, is known to strongly react and strip the adsorbed oxygen following the O_2 plasma step in each cycle.[31] Again, this is confirmed with our XPS analysis, where the peaks of O_2+H_2 PEALD Pt are shifted less toward higher binding energies than those of O_2 PEALD Pt. This two-stage plasma process, however, is still effective since the reactive O atoms removed from the H_2 plasma can be replenished in each cycle, thereby preparing the surface for the next Pt pulse.[59] Hydrogen molecules can then react with the metal oxide surface to form hydroxyl groups that reduce carbon levels at the interface and oxide inclusions within the Pt films. It is these impurities that promote the poor adhesion of noble metals such as Pt, noted for its inability to adhere to organic polymer films.[25]

To link adhesion and plasma treatments in PEALD Pt, recent work[32] has experimentally studied the effect on mechanical adhesion due to O_2 and O_2+H_2 in the PEALD of Pt. Described in the Supporting Information (Section S4), the result of introducing more plasma treatments was increasing peel strength—in direct agreement with the trend in our thermal results. Thus, we suspect that with a metal oxide surface the effect of our plasma treatments in a PEALD Pt interlayer is twofold: (i) the O_2 plasma generates stronger covalent bonds to the substrate and (ii) the H_2 plasma essentially strips the Pt of contaminants such as carbon. With such a process, the PEALD Pt can better adhere to the nucleation layer and become a more effective thermal conduction pathway. Although measurement uncertainties prevent us from separating the areal and chemical contributions, previous mechanical studies and the current thermal data provide semiquantitative insight into the mechanisms behind the apparent decrease in thermal resistance.

CONCLUSION

We have systematically studied metal−dielectric interfaces using ultrathin (40 cycle, ∼2 nm thick) PEALD Pt interlayers subjected to O_2 and O_2+H_2 plasma treatments. Quantitative values are given for the thermal resistance to conduction between PVD-Pt/PEALD-TiO_2 and PVD-Pt/PEALD-Al_2O_3/Si material systems by introducing these PEALD Pt interlayers at their interfaces. A consistent improvement in the effective thermal resistances between the metal−dielectric interfaces was observed, with reductions of up to 34% and 42% for TiO_2 and Al_2O_3 compared to control samples with no PEALD Pt at all. Although measurement uncertainties make it difficult to draw a definitive conclusion, increased interfacial bonding strength and additional contact area from nucleating islands of Pt are thought to have played a role. We suspect the effect of plasma treatments in a PEALD Pt interlayer is twofold: (i) the O_2 plasma generates stronger covalent bonds to the substrate and (ii) the H_2 plasma essentially strips the Pt of contaminants such as carbon, thus minimizing the mismatch in the vibrational spectra between the PVD Pt and PEALD Pt.

https://doi.org/10.1021/acsami.0c19197
ACS Appl. Mater. Interfaces XXXX, XXX, XXX−XXX

This study demonstrates that enhanced thermal transport across interfaces can be achieved with the inclusion of a thermal adhesive layer. Foundries and design engineers can leverage these insights to enhance performance and longevity of a multitude of electronic devices. The role of reaction chemistries, lower temperature deposition, and Pt cycle dependence can be further investigated to form a more complete understanding of heat conduction in contemporary deposition techniques such as PEALD.

■ ASSOCIATED CONTENT

Supporting Information

The Supporting Information is available free of charge at https://pubs.acs.org/doi/10.1021/acsami.0c19197.

Figures S1−S4 and Tables S1−S3 (PDF)

■ AUTHOR INFORMATION

Corresponding Author

Kenneth E. Goodson − *Department of Mechanical Engineering and Department of Materials Science and Engineering, Stanford University, Stanford, California 94305, United States; Huang Building, Dean's Office Suite, Stanford, California 94305, United States*; Email: goodson@stanford.edu

Authors

Heungdong Kwon − *Department of Mechanical Engineering, Stanford University, Stanford, California 94305, United States*; orcid.org/0000-0002-2548-3120

Christopher Perez − *Department of Mechanical Engineering, Stanford University, Stanford, California 94305, United States*; orcid.org/0000-0002-9628-2027

Hyojin K. Kim − *Department of Mechanical Engineering, Stanford University, Stanford, California 94305, United States*

Mehdi Asheghi − *Department of Mechanical Engineering, Stanford University, Stanford, California 94305, United States*

Woosung Park − *Division of Mechanical Systems Engineering, Sookmyung Women's University, Seoul 04310, South Korea*; orcid.org/0000-0001-9119-3781

Complete contact information is available at: https://pubs.acs.org/10.1021/acsami.0c19197

Author Contributions

[⊥]H.K. and C.P. contributed equally to this work. W.P. and K.E.G. conceived the idea. H.K. and C.P. characterized material properties, carried out image processing to estimate Pt coverage, and contributed to modelling the thermal boundary conductance and thermal conductivity as a function of thickness. H.J.K.K. helped with fabrication parameters and atomic layer deposition insights. All authors contributed to writing the manuscript. All authors have given approval to the final version of the manuscript.

Notes

The authors declare no competing financial interest.

■ ACKNOWLEDGMENTS

The authors acknowledge the financial support from the Semiconductor Research Corporation (Agreement No. 2012-OJ-2308 titled: Thermal Engineering, Optimization and Understanding the Physics of Electron and Phonon Conduction at Solid Interfaces) and a Kwanjeong Education Fellowship. Part of this work was performed at the Stanford Nano Shared Facilities (SNSF), supported by the National Science Foundation under Award ECCS-1542152. The authors acknowledge the use of the SNSF of Stanford University for sample preparation and characterization. The work performed by W.P. was supported by the Korea National Research Fund (NRF-2018R1C1B5086589).

■ REFERENCES

(1) Cahill, D. G.; Ford, W. K.; Goodson, K. E.; Mahan, G. D.; Majumdar, A.; Maris, H. J.; Merlin, R.; Phillpot, S. R. Nanoscale thermal transport. *J. Appl. Phys.* **2003**, *93*, 793.

(2) Pop, E. Energy dissipation and transport in nanoscale devices. *Nano Res.* **2010**, *3*, 147.

(3) Purkl, F.; English, T. S.; Yama, G.; Provine, J.; Samarao, A. K.; Feyh, A.; Kim, B.; O'Brien, G.; Ambacher, O.; Howe, R. T.; Kenny, T. W. Serpentine geometry for en-hanced performance of nanometer-thin platinum bolometers. *Transducers and Eurosensors XXVII: The 17th International Conference on Solid-State Sensors, Actuators and Microsystems, TRANSDUCERS and EUROSENSORS 2013*, 2013; pp 1507−1510.

(4) Khan, A. I.; Brenner, K.; Smithe, K. K.; Mleczko, M. J.; Pop, E. Large Temperature Coefficient of Resistance in Atomically Thin 2D Devices. *Device Research Conference - Conference Digest, DRC 2019*, 2019; pp 125−126.

(5) Semenov, O.; Vassighi, A.; Sachdev, M. Impact of self-heating effect on long-term reliability and performance degradation in CMOS circuits. *IEEE Trans. Device Mater. Reliab.* **2006**, *6*, 17−27.

(6) Pop, E.; Varshney, V.; Roy, A. K. Thermal properties of graphene: Fundamentals and applications. *MRS Bull.* **2012**, *37*, 1273−1281.

(7) Yalon, E.; McClellan, C. J.; Smithe, K. K.; Muñoz Rojo, M.; Xu, R. L.; Suryavanshi, S. V.; Gabourie, A. J.; Neumann, C. M.; Xiong, F.; Farimani, A. B.; Pop, E. Energy Dissipation in Monolayer MoS_2 Electronics. *Nano Lett.* **2017**, *17*, 3429−3433.

(8) Collins, K. C.; Chen, S.; Chen, G. Effects of surface chemistry on thermal conductance at aluminum-diamond interfaces. *Appl. Phys. Lett.* **2010**, *97*, 9−12.

(9) Hopkins, P. E.; Baraket, M.; Barnat, E. V.; Beechem, T. E.; Kearney, S. P.; Duda, J. C.; Robinson, J. T.; Walton, S. G. Manipulating thermal conductance at metal-graphene contacts via chemical functionalization. *Nano Lett.* **2012**, *12*, 590−595.

(10) Losego, M. D.; Grady, M. E.; Sottos, N. R.; Cahill, D. G.; Braun, P. V. Effects of chemical bonding on heat transport across interfaces. *Nat. Mater.* **2012**, *11*, 502−506.

(11) O'Brien, P. J.; Shenogin, S.; Liu, J.; Chow, P. K.; Laurencin, D.; Mutin, P. H.; Yamaguchi, M.; Keblinski, P.; Ramanath, G. Bonding-induced thermal conductance enhancement at inorganic hetero-interfaces using nanomolecular monolayers. *Nat. Mater.* **2013**, *12*, 118−122.

(12) Kaur, S.; Raravikar, N.; Helms, B. A.; Prasher, R.; Ogletree, D. F. Enhanced thermal transport at covalently functionalized carbon nanotube array interfaces. *Nat. Commun.* **2014**, *5*, 3082.

(13) Monachon, C.; Weber, L.; Dames, C. Thermal Boundary Conductance: A Materials Science Perspective. *Annu. Rev. Mater. Res.* **2016**, *46*, 433−463.

(14) Foley, B. M.; Hernández, S. C.; Duda, J. C.; Robinson, J. T.; Walton, S. G.; Hopkins, P. E. Modifying Surface Energy of Graphene via Plasma-Based Chemical Functionalization to Tune Thermal and Electrical Transport at Metal Interfaces. *Nano Lett.* **2015**, *15*, 4876−4882.

(15) Walton, S. G.; Foley, B. M.; Hernández, S. C.; Boris, D. R.; Baraket, M.; Duda, J. C.; Robinson, J. T.; Hopkins, P. E. Plasma-based chemical functionalization of graphene to control the thermal transport at graphene-metal interfaces. *Surf. Coat. Technol.* **2017**, *314*, 148−154.

(16) Potts, S. E.; Kessels, W. M. Energy-enhanced atomic layer deposition for more process and precursor versatility. *Coord. Chem. Rev.* **2013**, *257*, 3254−3270.
(17) Johnson, R. W.; Hultqvist, A.; Bent, S. F. A brief review of atomic layer deposition: From fundamentals to applications. *Mater. Today* **2014**, *17*, 236−246.
(18) Erkens, I. J.; Verheijen, M. A.; Knoops, H. C.; Keuning, W.; Roozeboom, F.; Kessels, W. M. Plasma-assisted atomic layer deposition of conformal Pt films in high aspect ratio trenches. *J. Chem. Phys.* **2017**, *146*, 052818.
(19) Youssef, S.; Podlecki, J.; Al Asmar, R.; Sorli, B.; Cyril, O.; Foucaran, A. MEMS scanning calorimeter with serpentine-shaped platinum resistors for characterizations of microsamples. *J. Microelectromech. Syst.* **2009**, *18*, 414−423.
(20) Ekkels, P.; Rottenberg, X.; Puers, R.; Tilmans, H. A. Evaluation of platinum as a structural thin film material for RF-MEMS devices. *J. Micromech. Microeng.* **2009**, *19*, 065010.
(21) Campbell, C. T. Metal films and particles on oxide surfaces: Structural, electronic and chemisorptive properties. *J. Chem. Soc., Faraday Trans.* **1996**, *92*, 1435−1445.
(22) Knoops, H. C.; MacKus, A. J.; Donders, M. E.; Van De Sanden, M. C.; Notten, P. H.; Kessels, W. M. Remote plasma ALD of platinum and platinum oxide films. *Electrochem. Solid-State Lett.* **2009**, *12*, 34−37.
(23) Ono, L. K.; Croy, J. R.; Heinrich, H.; Roldan Cuenya, B. Oxygen chemisorption, formation, and thermal stability of Pt oxides on Pt nanoparticles supported on SiO_2/Si(001): Size effects. *J. Phys. Chem. C* **2011**, *115*, 16856−16866.
(24) Baker, L.; Cavanagh, A. S.; Seghete, D.; George, S. M.; MacKus, A. J.; Kessels, W. M.; Liu, Z. Y.; Wagner, F. T. Nucleation and growth of Pt atomic layer deposition on Al_2O_3 substrates using (methylcyclopentadienyl)-trimethyl platinum and O_2 plasma. *J. Appl. Phys.* **2011**, *109*, 084333.
(25) Leskelä, M.; Ritala, M. Atomic Layer Deposition Chemistry: Recent Developments and Future Challenges. *Angew. Chem., Int. Ed.* **2003**, *42*, 5548−5554.
(26) Setthapun, W.; Williams, W. D.; Kim, S. M.; Feng, H.; Elam, J. W.; Rabuffetti, F. A.; Poeppelmeier, K. R.; Stair, P. C.; Stach, E. A.; Ribeiro, F. H.; Miller, J. T.; Marshall, C. L. Genesis and evolution of surface species during Pt atomic layer deposition on oxide supports characterized by in situ XAFS analysis and water-gas shift reaction. *J. Phys. Chem. C* **2010**, *114*, 9758−9771.
(27) Vitos, L.; Ruban, A. V.; Skriver, H. L.; Kollár, J. The surface energy of metals. *Surf. Sci.* **1998**, *411*, 186−202.
(28) Baker, L.; Cavanagh, A. S.; Yin, J.; George, S. M.; Kongkanand, A.; Wagner, F. T. Growth of continuous and ultrathin platinum films on tungsten adhesion layers using atomic layer deposition techniques. *Appl. Phys. Lett.* **2012**, *101*, 111601.
(29) Kim, H. J. K.; Kaplan, K. E.; Schindler, P.; Xu, S.; Winterkorn, M. M.; Heinz, D. B.; English, T. S.; Provine, J.; Prinz, F. B.; Kenny, T. W. Electrical Properties of Ultrathin Platinum Films by Plasma-Enhanced Atomic Layer Deposition. *ACS Appl. Mater. Interfaces* **2019**, *11*, 9594−9599.
(30) Park, W.; Sood, A.; Park, J.; Asheghi, M.; Sinclair, R.; Goodson, K. E. Enhanced Thermal Conduction Through Nanostructured Interfaces. *Nanoscale Microscale Thermophys. Eng.* **2017**, *21*, 134−144.
(31) English, T. S. Freestanding Nanostructured Sensors Fabricated by Atomic Layer Deposition. Ph.D. Thesis, Stanford University, 2016.
(32) Winterkorn, M. M. Applications of Atomic Layer Deposition for Next-Generation Nanoscale Devices. Ph.D. Thesis, Stanford University, 2019.
(33) Kim, S. K.; Hoffmann-Eifert, S.; Reiners, M.; Waser, R. Relation Between Enhancement in Growth and Thickness-Dependent Crystallization in ALD TiO_2 Thin Films. *J. Electrochem. Soc.* **2011**, *158*, D6.
(34) Jakschik, S.; Schroeder, U.; Hecht, T.; Gutsche, M.; Seidl, H.; Bartha, J. W. Crystallization behavior of thin ALD-Al_2O_3 films. *Thin Solid Films* **2003**, *425*, 216−220.
(35) Ahn, C.; Fong, S. W.; Kim, Y.; Lee, S.; Sood, A.; Neumann, C. M.; Asheghi, M.; Goodson, K. E.; Pop, E.; Wong, H. S. Energy-Efficient Phase-Change Memory with Graphene as a Thermal Barrier. *Nano Lett.* **2015**, *15*, 6809−6814.
(36) Sood, A.; Cho, J.; Hobart, K. D.; Feygelson, T. I.; Pate, B. B.; Asheghi, M.; Cahill, D. G.; Goodson, K. E. Anisotropic and inhomogeneous thermal conduction in suspended thin-film polycrystalline diamond. *J. Appl. Phys.* **2016**, *119*, 175103.
(37) Cahill, D. G. Analysis of heat flow in layered structures for time-domain thermoreflectance. *Rev. Sci. Instrum.* **2004**, *75*, 5119−5122.
(38) Gundrum, B. C.; Cahill, D. G.; Averback, R. S. Thermal conductance of metal-metal interfaces. *Phys. Rev. B: Condens. Matter Mater. Phys.* **2005**, *72*, 245426.
(39) Arblaster, J. W. The thermodynamic properties of platinum on ITS-90. *CALPHAD: Comput. Coupling Phase Diagrams Thermochem.* **1995**, *19*, 327−337.
(40) Chase, M. J. NIST-JANEF Thermochemical Tables, 4th ed. *Journal of Physical Chemistry and Chemical Reference Data Monographs or Supplements* **1998**, *9*, 1−1951.
(41) Gaskins, J. T.; et al. Review—Investigation and Review of the Thermal, Mechanical, Electrical, Optical, and Structural Properties of Atomic Layer Deposited High- k Di- electrics: Beryllium Oxide, Aluminum Oxide, Hafnium Oxide, and Aluminum Nitride. *ECS J. Solid State Sci. Technol.* **2017**, *6*, N189−N208.
(42) Scott, E. A.; Gaskins, J. T.; King, S. W.; Hopkins, P. E. Thermal conductivity and thermal boundary resistance of atomic layer deposited high-k dielectric aluminum oxide, hafnium oxide, and titanium oxide thin films on silicon. *APL Mater.* **2018**, *6*, 058302.
(43) DeCoster, M. E.; Meyer, K. E.; Piercy, B. D.; Gaskins, J. T.; Donovan, B. F.; Giri, A.; Strnad, N. A.; Potrepka, D. M.; Wilson, A. A.; Losego, M. D.; Hopkins, P. E. Density and size effects on the thermal conductivity of atomic layer deposited TiO_2 and Al_2O_3 thin films. *Thin Solid Films* **2018**, *650*, 71−77.
(44) Slack, G. A.; Glassbrenner, C. J. Thermal conductivity of Si and Ge from 3K to the melting point. *Phys. Rev.* **1964**, *134*, A1058−A1069.
(45) Liu, J.; Zhu, J.; Tian, M.; Gu, X.; Schmidt, A.; Yang, R. Simultaneous measurement of thermal conductivity and heat capacity of bulk and thin film materials using frequency-dependent transient thermoreflectance method. *Rev. Sci. Instrum.* **2013**, *84*, 034902.
(46) Lee, S. M.; Cahill, D. G. Heat transport in thin dielectric films. *J. Appl. Phys.* **1997**, *81*, 2590−2595.
(47) Yang, J.; Ziade, E.; Maragliano, C.; Crowder, R.; Wang, X.; Stefancich, M.; Chiesa, M.; Swan, A. K.; Schmidt, A. J. Thermal conductance imaging of graphene contacts. *J. Appl. Phys.* **2014**, *116*, 023515.
(48) Ziade, E.; Goni, M.; Sato, T.; Czubarow, P.; Schmidt, A. J. Thermal conductance of nanoscale Langmuir-Blodgett films. *Appl. Phys. Lett.* **2015**, *107*, 221603.
(49) Yang, F.; Dames, C. Mean free path spectra as a tool to understand thermal conductivity in bulk and nanostructures. *Phys. Rev. B: Condens. Matter Mater. Phys.* **2013**, *87*, 035437.
(50) Gorham, C. S.; Hattar, K.; Cheaito, R.; Duda, J. C.; Gaskins, J. T.; Beechem, T. E.; Ihlefeld, J. F.; Biedermann, L. B.; Piekos, E. S.; Medlin, D. L.; Hopkins, P. E. Ion irradiation of the native oxide/silicon surface increases the thermal boundary conduc- tance across aluminum/silicon interfaces. *Phys. Rev. B: Condens. Matter Mater. Phys.* **2014**, *90*, 024301.
(51) Little, W. The transport of heat between dissimilar solids at low temperatures. *Can. J. Phys.* **1959**, *37*, 334−349.
(52) Swartz, E. T.; Pohl, R. O. Thermal boundary resistance. *Rev. Mod. Phys.* **1989**, *61*, 605−668.
(53) Dutton, D. H.; Brockhouse, B. N. Crystal Dynamics of Platinum by Inelastic Neutron Scattering. *Can. J. Phys.* **1972**, *50*, 422−422.
(54) Wilson, R. B.; Apgar, B. A.; Hsieh, W. P.; Martin, L. W.; Cahill, D. G. Thermal conductance of strongly bonded metal-oxide

https://doi.org/10.1021/acsami.0c19197
ACS Appl. Mater. Interfaces XXXX, XXX, XXX−XXX

interfaces. *Phys. Rev. B: Condens. Matter Mater. Phys.* **2015**, *91*, 115414.
(55) Hu, M.; Keblinski, P.; Schelling, P. K. Kapitza conductance of silicon-amorphous polyethylene interfaces by molecular dynamics simulations. *Phys. Rev. B: Condens. Matter Mater. Phys.* **2009**, *79*, 104305.
(56) Hu, L.; Zhang, L.; Hu, M.; Wang, J. S.; Li, B.; Keblinski, P. Phonon interference at self-assembled monolayer interfaces: Molecular dynamics simulations. *Phys. Rev. B: Condens. Matter Mater. Phys.* **2010**, *81*, 235427.
(57) Shenogina, N.; Godawat, R.; Keblinski, P.; Garde, S. How wetting and adhesion affect thermal conductance of a range of hydrophobic to hydrophilic aqueous interfaces. *Phys. Rev. Lett.* **2009**, *102*, 156101.
(58) Giri, A.; Braun, J. L.; Hopkins, P. E. Implications of interfacial bond strength on the spectral contributions to thermal boundary conductance across solid, liquid, and gas interfaces: A molecular dynamics study. *J. Phys. Chem. C* **2016**, *120*, 24847.
(59) MacKus, A. J.; Leick, N.; Baker, L.; Kessels, W. M. Catalytic combustion and dehydrogenation reactions during atomic layer deposition of platinum. *Chem. Mater.* **2012**, *24*, 1752−1761.

https://doi.org/10.1021/acsami.0c19197
ACS Appl. Mater. Interfaces XXXX, XXX, XXX−XXX